Laboratory generation of internal waves from sinusoidal topography

D.A. Aguilar[a], B.R. Sutherland[a,*], D.J. Muraki[b]

[a]*Department of Mathematical and Statistical Sciences, University of Alberta, Edmonton, Alta., Canada T6G 2G1*
[b]*Department of Mathematics, Simon Fraser University, Burnaby, BC, Canada V5A 1S6*

Abstract

In the first of a multistage process to understand the generation of internal waves from rough topography, we have performed laboratory experiments to study wave generation over and in the lee of small- and large-amplitude sinusoidal topography. The model hills are towed at a range of speeds along the surface of a uniformly salt-stratified fluid. The experiments show that internal waves are generated not only by flow over the hills but also by flow over "boundary-trapped" lee waves and turbulent structures in the lee. Waves are visualized and their characteristics measured using a nonobtrusive optical technique called "synthetic schlieren". Experimental results are compared with the predictions of linear theory and Long's model. For low values of the excitation frequency, the internal wave frequencies are consistent with those predicted by linear theory. The wave amplitudes, however, are significantly lower than the hill amplitude, even for the small hills that have a maximum slope of 0.3. This indicates the importance of nonlinear processes, such as boundary layer separation, which act even for moderate hill slopes. When the excitation frequency exceeds the buoyancy frequency, internal waves are still excited in the lee of the topography, with frequency an approximately constant fraction of the buoyancy frequency. In these cases, boundary-trapped lee waves and turbulent structures are observed and couple with vertically propagating internal waves.
© 2006 Elsevier Ltd. All rights reserved.

Keywords: Internal gravity waves; Topographic generation; Abyssal ocean mixing; Laboratory experiments; Long's model

1. Introduction

Internal waves are generated whenever a stratified fluid is perturbed at a frequency below the natural frequency of vertical oscillation of the fluid (i.e. the buoyancy frequency). The waves subsequently propagate horizontally and vertically within the fluid, transporting energy and momentum away from their source. Eventually, waves may become unstable and break, depositing momentum and energy to the background flow.

In the ocean, internal waves are a significant source of mixing, which consequently redistributes heat and so may influence the Earth's climate (Ledwell et al., 2000; Rudnick et al., 2003). Recent observations in the deep ocean have shown that waves are generated most significantly by the flow of tides over the rough terrain of the ocean floor, such as seamounts, ridges, and canyons (New and

*Corresponding author. Tel.: +1 780 492 0573;
fax: +1 780 492 6826.

E-mail address: bruce.sutherland@ualberta.ca
(B.R. Sutherland).

DaSilva, 2002; Rudnick et al., 2003; St. Laurent et al., 2003). In many of these sites, energetic turbulence has been observed (Ledwell et al., 2000; Klymak and Gregg, 2004; Garabato et al., 2004) and presumably results directly as a consequence of flow over topography and wave breaking.

The characteristics of the internal wave field generated by flow over bottom topography depend on the observation time scale, as depicted in the schematic of Fig. 1. When tidal flows are observed on scales well above the inertial period, f^{-1}, (e.g., days and/or months), the waves radiate mainly at the fundamental frequency of the tide in both upstream and downstream directions. However, when the flows are observed over intermediate time-scales close to the buoyancy period, N^{-1}, (e.g., minutes and/or hours), the flow resembles uniform flow over topography and the waves propagate only in the upstream direction with phase speed $\sim U$ and frequency $\sim Uk$ relative to
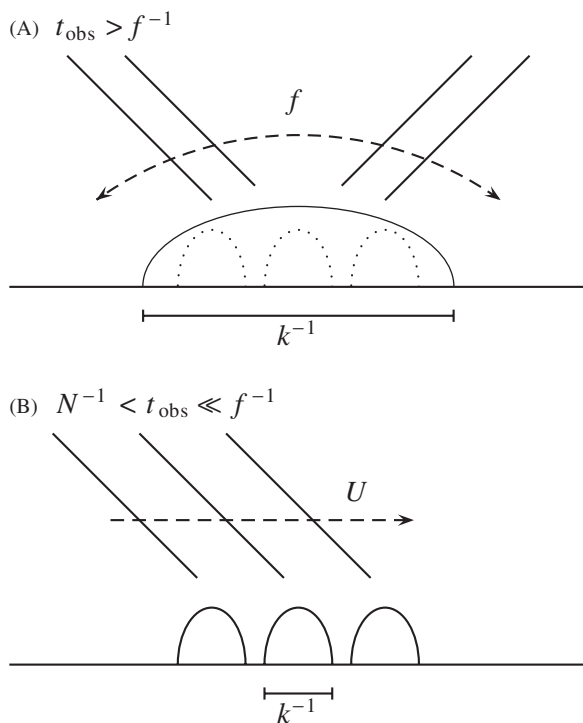

(A) $t_{\mathrm{obs}} > f^{-1}$

(B) $N^{-1} < t_{\mathrm{obs}} \ll f^{-1}$

Fig. 1. Different time-scales for observations of internal waves (adapted from Dohan, 2004):(A) on time-scales longer than the inertial period, tidal motion can be viewed as periodic and generates internal waves at approximately the fundamental frequency of the tides; (B) on time-scales less than the inertial period, tidal motion can be viewed locally as uniform flow over topography, with internal waves generated in only in the upstream direction.

the flow. Here, U is the tidal flow speed and k^{-1} is the horizontal length scale of the topography. N is the buoyancy frequency, which in the Boussinesq approximation, is given in terms of the background density, $\overline{\rho}(z)$, a characteristic density, ρ_0, and the acceleration due to gravity, g, by $N^2 = -(g/\rho_0)\mathrm{d}\overline{\rho}/\mathrm{d}z$.

St. Laurent and Garrett (2002) use the terms "internal tide" and "quasi-steady lee wave" to describe the two regimes illustrated in Figs. 1(A and B), respectively. The regimes are distinguished using the tidal excursion parameter, Uk/ω, which compares the length of the tidal excursion, U/ω, to the horizontal scale of the topography, k^{-1}, where ω is the tidal frequency. Thus, the "internal tide" regime is characterized by $Uk/\omega < 1$ and the "quasi-steady lee wave" regime by $Uk/\omega > 1$.

Another parameter used in classifying flow over bottom topography is the steepness parameter, $\varepsilon = s/\alpha$. Here s is the topographic slope defined as the ratio of the topographic height to length, $s = Hk$, and α is the slope of the wave beam, defined as the ratio of the horizontal to vertical wavenumbers, $\alpha = k_x/k_z$ ($= \omega/N$ for hydrostatic flow). In circumstances satisfying $\varepsilon < 1$, the waves are said to encounter "subcritical topography", whereas they encounter "supercritical topography" if $\varepsilon > 1$.

Much attention has been devoted to the "internal tide" regime using both subcritical and supercritical topography (e.g., recently by Llewellyn Smith and Young, 2002, 2003; Balmforth et al., 2002; St. Laurent and Garrett, 2002). Even so, the properties of internal tides generated at supercritical topography remain poorly understood (St. Laurent et al., 2003). Here, we discuss the situation depicted in Fig. 1(B), in which nonhydrostatic waves are generated from steady flow over topography. In such a case, there is no tidal frequency and so the parameter ε is insignificant and the mechanisms by which internal waves are generated from topography are poorly understood beyond the suppositions of linear and inviscid theories.

In particular, linear theory restricts predictions of topographically generated waves to those launched by smooth hills with small aspect ratios of topographic height to width, H/L. In such cases, theory predicts that propagating waves will be generated if the excitation frequency, ω_{exc}, is lower than the buoyancy frequency, N. Here, ω_{exc} is defined in terms of the flow speed, U, and the topographic wavelength, λ, (or equivalently the

wavenumber, $k = 2\pi/\lambda$) as

$$\omega_{\text{exc}} \equiv U\frac{2\pi}{\lambda} = Uk. \tag{1}$$

The ratio of excitation to buoyancy frequency defines a "horizontal" Froude number

$$Fr_{\text{h}} \equiv \frac{\omega_{\text{exc}}}{N} = \frac{Uk}{N}. \tag{2}$$

Thus, linear theory predicts that vertically propagating internal waves are generated if $Fr_{\text{h}} < 1$. This we refer to as subcritical flow, which should not be confused with subcritical topography. In this case the maximum vertical displacement, A_ξ, of the fluid due to waves equals $H/2$, half the peak-to-peak height of the hills. When $Fr_{\text{h}} > 1$, which we refer to as supercritical flow, the waves are termed "evanescent" meaning that the wave amplitude decays exponentially. Fr_{h} also provides a measure of hydrostatic balance, in particular the flow is hydrostatic if $Fr_{\text{h}} \ll 1$.

In addition to Fr_{h}, an equally important parameter for studying stratified flow over topography is the quantity NH/U, which is used as a measure of nonlinearity introduced by a finite topographic height. There is no standard symbol for this quantity in the literature and thus, in this paper, we will define a "vertical" Froude number by

$$Fr_{\text{v}}^{-1} \equiv \frac{NH}{U}. \tag{3}$$

Combining these two parameters gives $Fr_{\text{h}}Fr_{\text{v}}^{-1} = Hk$. Thus, the linear theory assumption can be summarized by the condition that $Hk \ll 1$. In the ocean, this is valid, for example, to describe tidal flow over mid-ocean ridge topography with subcritical slopes and occurring on long time scales (Lamb, 2004). However, it is not valid when modeling flow associated with supercritical oceanic trench systems such as the Hawaiian and Aleutian ridges (St. Laurent et al., 2003). It is therefore important to understand the limitations of applying results from linear theory to such circumstances. This paper will specifically examine the case of $Hk = 0.6$ and 1.2 on time-scales close to the buoyancy period.

Long's model extends linear theory to include waves generated by steady, inviscid flow over finite-amplitude topography, which does not include the nonlinear dynamics of boundary layer separation from steep slopes, flow stagnation in valleys or turbulence. In real situations, such nonlinear and unsteady effects can act to alter the generation of internal waves. The purpose of the present research is to use laboratory experiments to investigate the ways in which internal waves are generated from flow over and in the lee of finite-amplitude topography, including the nonlinear effects described above, and to determine the corresponding limitations of linear and inviscid theories.

Boundary layer separation occurs when fluid flowing over an obstacle encounters an adverse pressure gradient, which decelerates the fluid and causes the boundary layer to separate from the obstacle. In the context of flow over topography, this can occur on the lee-side slopes of both isolated and periodic hills provided that the flow is sufficiently energetic and/or the hills sufficiently steep.

According to Baines (1995), separation should occur for $NL_{\text{h}}/U < \pi$ ($Fr_{\text{h}} > 1$) and complete attachment for $NL_{\text{h}}/U > \pi$ ($Fr_{\text{h}} < 1$), where L_{h} is the half-width of the obstacle (whether isolated or part of a range). However, separation can still occur at lower Fr_{h} values, provided that Fr_{v}^{-1} and H/L_{h} are sufficiently high. This will be of particular interest in our experiments, which have relatively large values of H/L_{h} and $Fr_{\text{v}}^{-1} \sim 1$ (where $L_{\text{h}} = \lambda/2$ for sinusoidal topography). We hypothesize that for experiments with tall and steep topography, boundary layer separation will eventually become independent of Fr_{h}, being controlled predominately by Fr_{v}^{-1}.

When fluid separates from the lee-side slope of an isolated hill (or the last in a range of hills), the formation of a stationary, undulating shear layer downstream of the hill, sometimes called a "boundary-trapped" lee wave, may result. This is an example of what Baines (1995) calls "post-wave" separation. Beneath the crests of the lee waves lies either stagnant or mixed fluid, depending on the flow speed. Flow over these "fluidic" hills has been identified as a possible mechanism of internal wave generation (Sutherland, 2002).

Laboratory experiments performed by Sutherland (2002) examined stratified flow over a "smooth" step and showed that vertically propagating internal waves and boundary-trapped lee waves were generated with frequency a constant fraction of the buoyancy frequency, approximately $0.75N$ for $Fr_{\text{v}}^{-1} < 1$ and moderately smaller values for larger Fr_{v}^{-1}. Sutherland observed that the generation of internal waves was coupled to that of lee waves and suggested that this may be an important factor in mixing over rough topography in the ocean. This

study did not, however, capture the dynamics of the flow of fluid into and out of the valleys of topographic features such as mountain ridges on land or sea mounts and canyons on the ocean floor. The present research is thus an extension of this work to include the more complex dynamics of flow over, between, and in the lee of finite-amplitude sinusoidal hills.

In the case of periodic topography, through boundary layer separation, stagnant fluid may remain trapped within the valleys. The formation of stagnant fluid thus reduces the effective overall hill height for wave generation. The depth of these "blocked layers" increases slightly with increasing Fr_{v}^{-1} (Baines, 1995). Using numerical simulations, Welch et al. (2001) examined the formation and properties of blocked layers between finite-amplitude sinusoidal hills. They found that blocked layers were formed when Fr_{v}^{-1} exceeded a certain threshold, between 0.5 and 1. Also, once the hill height reached a certain threshold, the height of the blocked layer was found to increase linearly with H so as to achieve a relatively constant effective hill height, H_{eff}. The constancy of H_{eff} suggested that flow with background N and U could only sustain waves of a certain amplitude.

Turbulence above and in the lee of periodic topography may be created if the flow speed is sufficiently high and the topography sufficiently steep. There have been relatively few studies of turbulence (coherent or random) as a generation mechanism of internal waves (Linden, 1975; Carruthers and Hunt, 1986; Dohan and Sutherland, 2003). In a recent adaption of experiments by Linden (1975), Dohan and Sutherland (2003) examined the excitation of internal waves from random small-scale turbulent forcing above a stationary stratified fluid. Despite the random nature of the forcing, the resulting wave frequencies were found to lie in a narrow range. This same result was found in corresponding two-dimensional numerical simulations (Dohan, 2004).

Sutherland and Linden (1998) performed laboratory experiments to investigate the excitation of internal waves from a turbulent shear flow over a thin barrier. In their study, a coupling was observed between coherent turbulent structures shed in the lee of the barrier and the internal waves that radiated from the mixing region. In particular, internal waves were observed to propagate with the same length-scale and horizontal phase speed as disturbances at the base of the mixing region. Part

of the work presented here extends the research on turbulence generation to examine the situation of supercritical flow over sinusoidal topography and to determine the effects of turbulence created in the lee of topography upon wave generation.

In Section 2, we introduce the experimental set-up, including methods for wave visualization and techniques for determining wave properties such as frequency, wavenumber and amplitude. In Section 3, we present qualitative experimental observations, followed by quantitative results in Section 4. In Section 5, we introduce Long's theoretical model and its solution method, and we compare its predictions against our experimental findings. Discussion and conclusions are presented in Section 6.

2. Experimental methods

2.1. Apparatus

Experiments were performed in a glass tank having dimensions 197 cm long by 50 cm high by 17.5 cm wide. The tank was filled with uniformly salt-stratified water to a depth of approximately 27 cm. This was accomplished using the standard "double-bucket" technique (Oster, 1965). The background density field, $\overline{\rho}(z)$, was obtained by traversing a conductivity probe down through the tank before each experiment. A schematic illustrating the tank dimensions and a typical background density profile is given in Fig. 2(A). The buoyancy frequency was determined directly from the slope of the best-fit line to the density profile. With some exceptions, its typical value was $N = 1.10 \pm 0.02\,\mathrm{s}^{-1}$.

Although the fluid had finite depth, the experiments were performed over such short periods of time ($\sim 30-80\,\mathrm{s}$) that the vertically propagating internal waves did not reach the tank bottom before the experiments finished. Thus, the effect of the bottom boundary was negligible and the experiments effectively modeled wave propagation in an infinite-depth fluid.

Two spanwise uniform sinusoidal topographies of different peak-to-peak hill heights, $H = 1.3$ and 2.6 cm, were used. The topographies spanned four hill wavelengths with $\lambda = 13.7\,\mathrm{cm}$, giving relative hill heights of $H/\lambda \approx 0.1$ and 0.2, respectively. In this paper, the two topographies will be referred to as "small-amplitude" and "large-amplitude". Note that the small-amplitude hills are in fact quite large with $H/\lambda \approx 0.1$.

(A) Front view of tank and towing apparatus
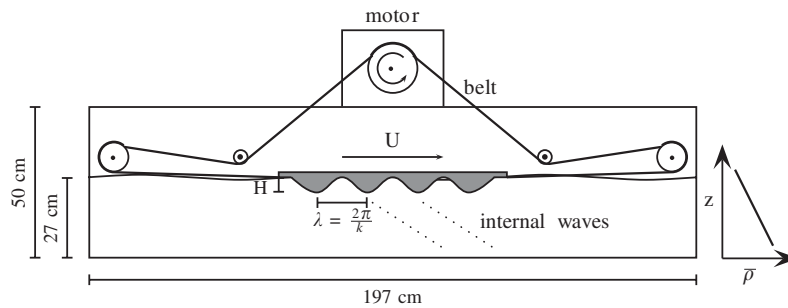
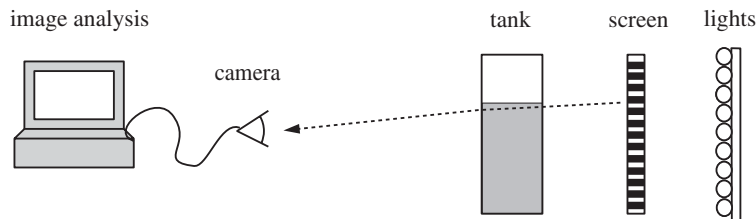(B) Side view of synthetic schlieren set-up

Fig. 2. (A) Front view of tank and towing apparatus. The motor is mounted above the tank. A belt is attached to the topography and runs around a series of pulleys. When the motor is turned on, the topography moves from left to right at an approximately constant speed, thus exciting internal waves. (B) Side view of the experimental configuration for the synthetic schlieren technique. The technique records the distortion of the image of horizontal lines due to density fluctuations within the tank. The density fluctuations are the result of internal wave motion.

To simulate uniform flow over topography, model sinusoidal hills were towed along the surface of the fluid at an approximately constant speed. This was achieved using a towing apparatus consisting of a motor, five pulleys, and a belt that was fixed to the model topography (see Fig. 2(A)). Because the density difference between the salt water at the top and bottom of the tank was small compared to the density of the water itself, the fluid was Boussinesq. Hence there is no dynamic difference between waves propagating downward from topography towed along the top of the tank and waves propagating upward from topography towed along the bottom of the tank. The model hills were towed at speeds ranging from $U = 0.9 - 4.9\,\mathrm{cm\,s^{-1}}$. The corresponding horizontal and inverse vertical Froude numbers ranged from $Fr_h = 0.2 - 2.0$ and $Fr_v^{-1} = 0.29 - 6.07$.

As Fr_h increased, the flow between and in the lee of the hills underwent a transition to turbulence, which altered the generation of waves from direct topographic generation to indirect turbulence generation via flow over coherent turbulent structures in the lee of the topography. The relationship between the turbulent structures and the corresponding internal waves is examined in Section 3.2.

The Reynolds number, based on L, ranged from $Re_L \approx 1000 - 5000$. Although significantly smaller than typical ocean values $\sim 10^9$, the experimental values are still large enough that viscous effects should be important only insofar as boundary layer separation and turbulence damping time scales are concerned. Boundary layer separation occurs even for high Reynolds number geophysical flows if the topography is sufficiently steep and internal wave generation by turbulence is affected by integral length and time scales, not the viscous scales of turbulence. Therefore, the experimental results should be relevant to realistic circumstances in the ocean.

The experiments were recorded using a digital camera situated approximately 340 cm in front of the tank. The recorded images in the x–z plane were analyzed using the image processing software package, Digimage (Dalziel et al., 2000). The analysis of these images is described further in the following subsections.

2.2. Synthetic schlieren technique

The synthetic schlieren technique was used to measure nonobtrusively the two-dimensional internal wave field as it evolved in time (Dalziel et al., 2000). The technique is based on how light is deflected to a greater or lesser degree as it passes, respectively through stronger or weaker density gradients. The experimental configuration is illustrated schematically in Fig. 2(B).

A 50 cm long by 30 cm high translucent screen of horizontal black and white lines was placed behind the tank. Situated behind the screen was a bank of fluorescent lights, which illuminated the screen. The field-of-view of the camera was set such that a minimum of eight pixels covered the width of a single horizontal line. This generally resulted in a field-of-view measuring approximately 25 cm in the

horizontal and 20 cm in the vertical, sufficiently large to capture the internal waves generated near the topography. A sample field-of-view is given in Fig. 3(A), which shows an image taken immediately before the start of an experiment. The experiment used the large-amplitude hills towed at a moderate speed, hereafter referred to as the featured experiment.

When internal waves move within the tank, they stretch and compress isopycnal surfaces, thereby changing the local density gradient. This consequently changes the local gradient of the index of refraction of the fluid so that the horizontal lines appear to be displaced. Fig. 3(B) shows an image taken during the featured experiment, after the hills have been towed through a distance of one hill wavelength. The distortion of the horizontal lines compared to the initial image in Fig. 3(A) is barely
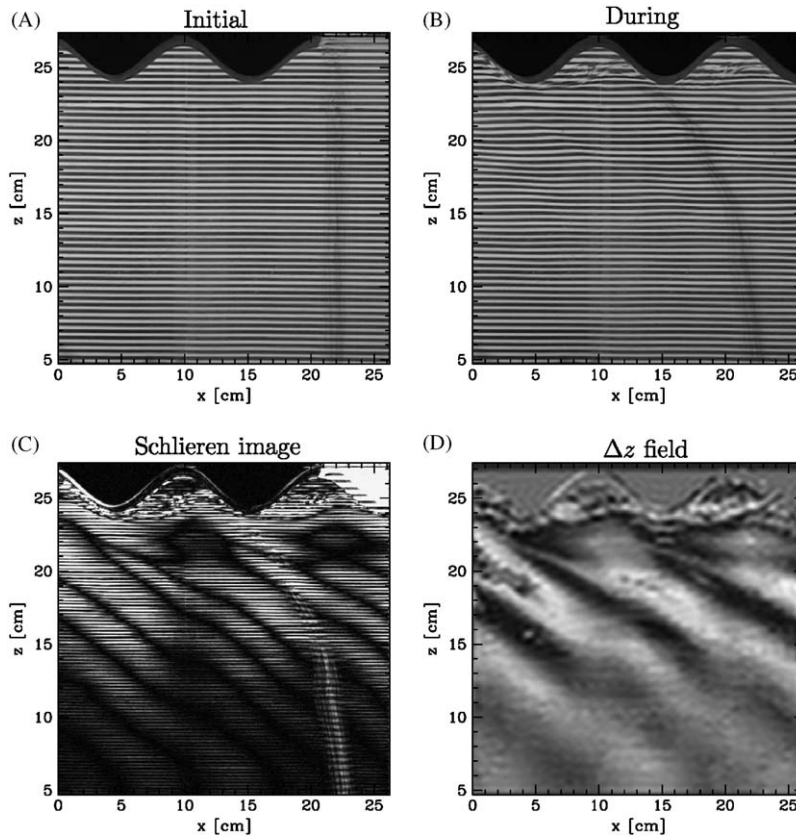

Fig. 3. Snapshot images taken from the featured experiment (A) before the start of the experiment and (B) after the hills have been towed through a distance of one hill wavelength. Subtracting intensities in (A) from (B) and scaling yields the qualitative synthetic schlieren image (C). The corresponding Δz field is shown in (D), where the grey-scale range is between -0.08 and 0.08 cm. The vertical grey line at $x \simeq 22$ cm in (A) and the tilted line in (B) is the result of dye laid down by potassium permanganate crystals. This shows up as a vertical white streak in (C) but is filtered in computing Δz, as shown in (D). Parameter values for this experiment are $H = 2.6$ cm, $U = 0.97$ cm s^{-1}, $Fr_{\mathrm{h}} = 0.41$, $Fr_{\mathrm{v}}^{-1} = 2.94$, $Hk = 1.2$.

visible. By taking the difference between the images in Figs. 3(A and B), we obtain the qualitative synthetic schlieren image given in Fig. 3(C). The intensity difference between the images is multiplied by a factor of 2 to reveal clearly the regions having the greatest displacement, namely the wave crests and troughs.

By measuring the displacement of the lines from their initial position, $\Delta z(x, z, t)$, the change in the squared buoyancy frequency can be directly calculated:

$$\Delta N^2(x, z, t) = -\frac{g}{\rho_0}\frac{d\rho}{dz} \simeq \alpha \Delta z(x, z, t), \qquad (4)$$

where α is a constant that depends on the tank width, the distance from the tank to the screen, the indices of refraction of salt water and air, and the gravitational constant g (Sutherland et al., 1999). In our experiments, $\alpha = 6.5\,\mathrm{s}^{-2}\,\mathrm{cm}^{-1}$. A sample Δz field is shown in Fig. 3(D). Because (4) assumes disturbances across the tank are spanwise uniform, the computed wave field is reliable only away from the mixing near the hilltops.

From such images, the horizontal and vertical wavelengths can be estimated by measuring the horizontal and vertical distances between successive wave crests or troughs. For example, from Fig. 3, $\lambda_x \approx 11\,\mathrm{cm}$ and $\lambda_z \approx 7\,\mathrm{cm}$, which correspondingly gives wavenumber components $k_x \approx 0.57\,\mathrm{cm}^{-1}$ and $k_z \approx 0.90\,\mathrm{cm}^{-1}$. Rigorous quantitative methods for determining these quantities are presented in Section 4.1. Consequently, the angle of wave propagation to the vertical, Θ, (or equivalently, the angle formed by lines of constant phase with the vertical) can be estimated using the relation

$$\tan\Theta = \frac{k_z}{k_x}. \qquad (5)$$

For this example, $\Theta \approx 58^\circ$. Alternately, the angle can be estimated from the relative wave frequency using the dispersion relation

$$\cos\Theta = \omega/N. \qquad (6)$$

In addition to calculating ΔN^2, the time-derivative of the squared buoyancy frequency, N_t^2, can be calculated by measuring the displacement of the horizontal lines between two short successive times. The time interval used in our experiments was $\Delta t = n/30\,\mathrm{s}$, where $n = 1, 2, 3, 4$, or 5 depending on the towing speed. In all cases, Δt was much smaller than a typical wave period ($T \approx 10\,\mathrm{s}$),

but large enough to give a substantial signal from the waves.

From the ΔN^2 field, the vertical and horizontal velocity fields can be estimated using linear theory. Similarly, the vertical displacement field, ξ, can be estimated from the N_t^2 field. These estimates are reasonable for small-amplitude disturbances up to $A_\xi/\lambda_x \approx 0.2$. For the purposes of performing qualitative and quantitative analyses, the N_t^2 field was preferred for three reasons: it was in phase with the vertical displacement field, ξ; it could be determined even for large-amplitude waves, which significantly distorted the background image; and it filtered long time-scale changes, thus capturing the signal from propagating waves uncontaminated by the development of columnar modes.

2.3. Time series analyses

Time series of N_t^2 were used both to visualize the internal wave field and to quantitatively determine fundamental wave properties such as frequency, wavenumber, amplitude. Vertical time series, $N_t^2(z, t)$, illustrate the time evolution of a vertical slice through images of an experiment at a single horizontal location, whereas horizontal time series, $N_t^2(x, t)$, illustrate the time evolution of a horizontal slice at a single vertical location. Fig. 4 shows sample vertical and horizontal time series for the featured experiment. Here, the horizontal time series has been reconstructed using 18 equally spaced vertical time series images spanning the entire field-of-view. The images have been enhanced using low-pass filters to remove high-frequency thermal and electronic noise and using Fourier filters to remove low-frequency thermal variations. From Fig. 4(A), lines of constant phase move upwards as times evolves, consistent with the linear theory prediction that energy is transported downwards and away from the hills. Fig. 4(B) shows that the waves move from left to right, in the same direction toward which the topography is towed.

The frequencies and wavenumbers of the internal waves were determined from the peaks of the power spectra of the N_t^2 time series (see Section 4.1). The half peak-to-peak amplitude of the N_t^2 field, $A_{N_t^2}$, was determined by taking the root-mean-squared average in time and then multiplying by a factor of $\sqrt{2}$. For the purpose of making quantitative comparisons among experiments, a characteristic wave amplitude value was obtained by spatially averaging the root-mean-squared value. The
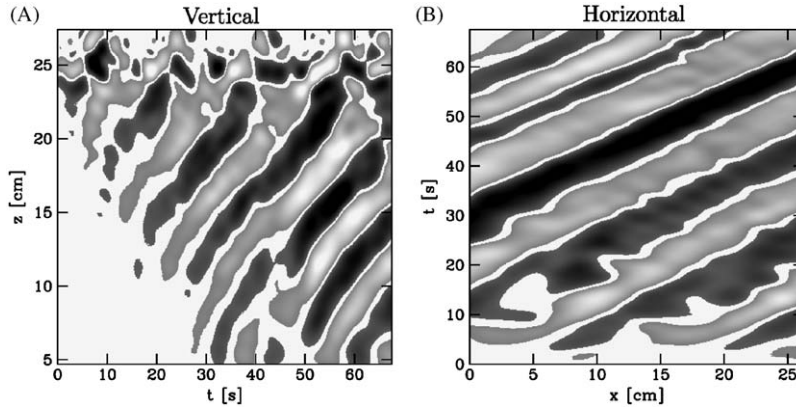
Fig. 4. Sample (A) vertical and (B) horizontal time series of N_t^2 for the featured experiment. Time $t = 0$ s corresponds to the start of towing. The vertical time series is taken at a horizontal location corresponding to the initial position of the first hill crest (at $x = 15$ cm in Fig. 3(A)). The horizontal time series is taken at a vertical location 5 cm below the hill crest. The light and dark bands are the wave crests and troughs, which move upwards and to the right as time evolves and the waves propagate downward and to the right. The grey-scale is arbitrary for the purpose of this figure.

averaging window was selected to isolate the waves and generally extended across a minimum of one wavelength in both directions, beginning at least 5 cm below the peak of the topography (see Section 4.1 for further details). This location was sufficiently far from the local mixing region where the schlieren technique did not accurately measure N_t^2. The amplitude of vertical displacement, A_ξ, was estimated from $A_{N_t^2}$ using the relation for Boussinesq linear plane waves in a uniformly stratified fluid, given by

$$A_{N_t^2} = k_x N^3 \sin \Theta A_\xi,$$
$$= 2\pi N^3 \sqrt{1 - Fr_h^2} \frac{A_\xi}{\lambda_x} \tag{7}$$

in which Θ is given by (6) and Fr_h is given by (2).

3. Qualitative observations

3.1. Internal wave fields

Recall that linear theory predicts propagating waves are generated if $Fr_h < 1$ and the waves are evanescent otherwise. For linear theory to be valid, we require both $Fr_v^{-1} \ll 1$ and $Hk = Fr_h/Fr_v \ll 1$. Fig. 5 summarizes the experiments we have performed in terms of Fr_h and Fr_v^{-1}. We have focused on the weakly ($Fr_v^{-1} \lesssim 1$) and strongly ($Fr_v^{-1} > 1$) nonlinear regime because it lies beyond well-established theory and because for very small-amplitude hills, the generated internal waves are
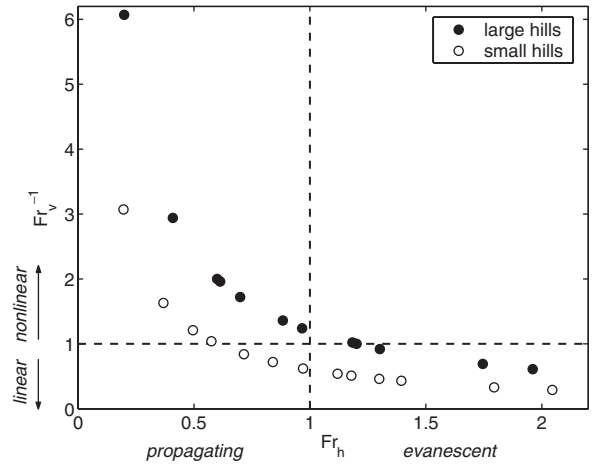

Fig. 5. Summary of experiments in terms of horizontal and inverse vertical Froude numbers. Linear and nonlinear regimes are identified using Fr_v^{-1}, while propagating and evanescent waves are identified using Fr_h. The open circles are for the small-amplitude hills with relative amplitude $(H/2)/\lambda \simeq 0.047$ or $Hk \simeq 0.6$, and the closed circles are for the large-amplitude hills with $(H/2)/\lambda = 0.095$ or $Hk \simeq 1.2$.

too small to be accurately measured above signal noise.

To illustrate the properties of internal waves as they depend on towing speed and topographic height, we compare four vertical time series of N_t^2. Two are taken from experiments using the small-amplitude hills and two from those using the large-amplitude hills (see Fig. 6). The vertical time series are taken at a horizontal location corresponding to
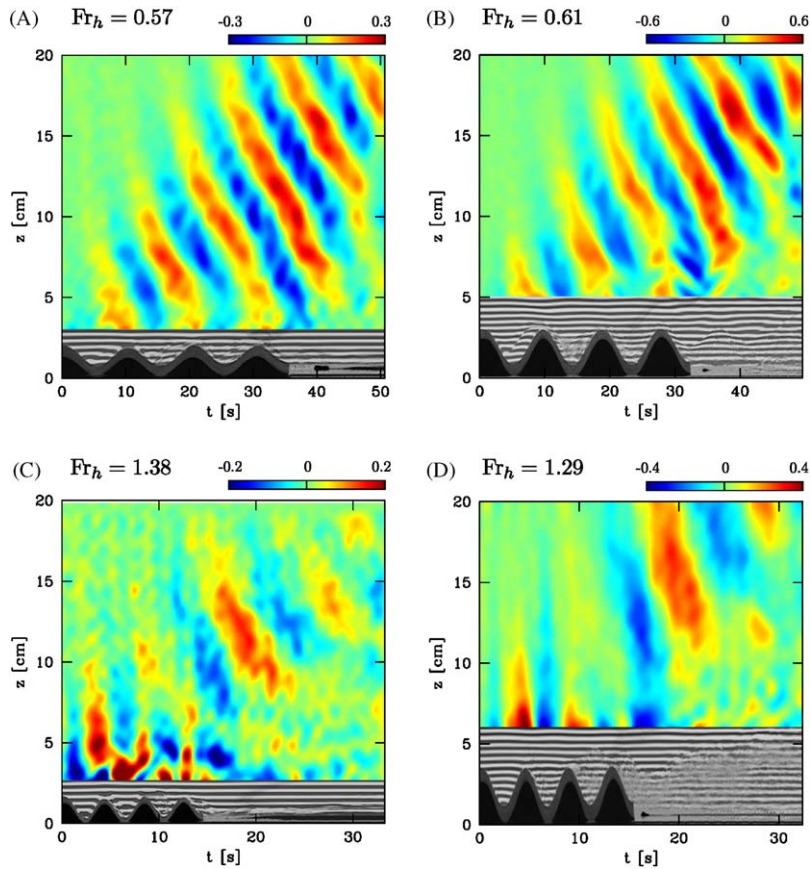
Fig. 6. Vertical time series of N_t^2 [s^{-3}] for the small- and large-amplitude hills for the cases of $Fr_h < 1$ (A,B) and $Fr_h > 1$ (C,D). Vertical time series of the near-hill region of the raw images are superimposed to help visualize the correlation of the vertically-propagating internal waves relative to the topography and to observe boundary layer separation and boundary-trapped lee waves (see Section 3.2).

the initial position of the first hill crest, thus capturing the movement of the remaining three hill crests through this location. The range of colour contours for the large-hill images is twice that for the small-hill images, thus highlighting the amplitude relative to the topographic height.

Figs. 6(A and B) presents cases where $Fr_h < 1$ while Figs. 6(C and D) presents cases where $Fr_h > 1$. For conceptual convenience in imagining flow over bottom topography, the images have been flipped vertically and the z-axis has been rescaled such that $z = 0$ corresponds to the bottom of the topography. The near-hill region of the vertical time series of the raw image is superimposed at the bottom of the frame. This is done to reveal flow structures in the valleys and lee of topography and so illustrate the relationships between the excitation mechanisms and the resulting wave fields. In any case, quantitative schlieren cannot be used to compute wave

amplitudes in this region where the image of horizontal lines is often blurred by turbulence.

The regularity of the wave field for $Fr_h < 1$ is evident for both hills in Figs. 6(A and B). Comparing the horizontal distance between successive hilltops to the distance between successive crests or troughs, they are approximately the same. This is consistent with the expectation based on linear theory that the internal waves generated in these cases have frequencies that match the excitation frequencies. Two subtle, yet important, distinctions can be made between the images in Figs. 6(A and B). The first concerns waves generated directly over the hills, in which case the amplitude of the wave field relative to the hill height is slightly greater in the small-amplitude hill experiments. The second concerns the waves in the lee of the last hills, in which case a significant increase in amplitude is evident for the large hills and only a slight increase

for the small hills. This increase is associated with the flow structure in the lee of the last hill (see Fig. 6(B)) and is described in the next subsection.

In Figs. 6(C and D), corresponding to super-critical wave excitation ($Fr_h > 1$), propagating internal waves are not generated directly over the topography but are observed, however, in the lee. These lee waves have longer periods, despite their rapid period of excitation. The generated wave frequencies, determined from the distance between successive crests or troughs in Figs. 6(C and D), are approximately equal, even though the hill heights, towing speeds, and relative amounts of turbulence are different. There is some evidence of high frequency, evanescent waves in the initial stages of the experiments. However, these motions decay before the hills pass and do not persist in the lee.

3.2. Boundary layer separation

In this subsection, we qualitatively examine the region near and in the lee of the hills in order to understand the generation of the previously presented wave fields. We select six sample vertical time series of the near-topography region, which illustrate well the effects of increasing Fr_h and H.

Figs. 7(A and B) compares images having $Fr_h < 1$. For the small hills, there is little distortion of the horizontal lines. However, for the large hills, there are significant distortions both between the hills and directly in their lee. In particular, in Fig. 7(B) the flow over and between the hills ($t \approx 0-20$ s) separates from the lee-side slope of the hills, forming stagnant patches of fluid between the hills and reducing the effective hill height. This helps to explain the decreased relative wave amplitude observed in Fig. 6(B) compared to 6(A) for $t \approx 0-25$ s.

In the lee of the last hill ($t \approx 20-40$ s) shown in Fig. 7(B), the distortion of the lines reveals an undular shear layer, which begins where the boundary layer separates from the lee-side of the last hill. This undular shear layer, or boundary-trapped lee wave, is similar to that observed downstream of a single "Witch of Agnesi" hill in three experiments by Baines and Hoinka (1985) (with parameter values $Fr_v^{-1} = 0.8$, 0.9, and 1.1 based on total hill height and, respectively, $Fr_h = 3.2$, 2.8, and 2.3 based on hill half-width),
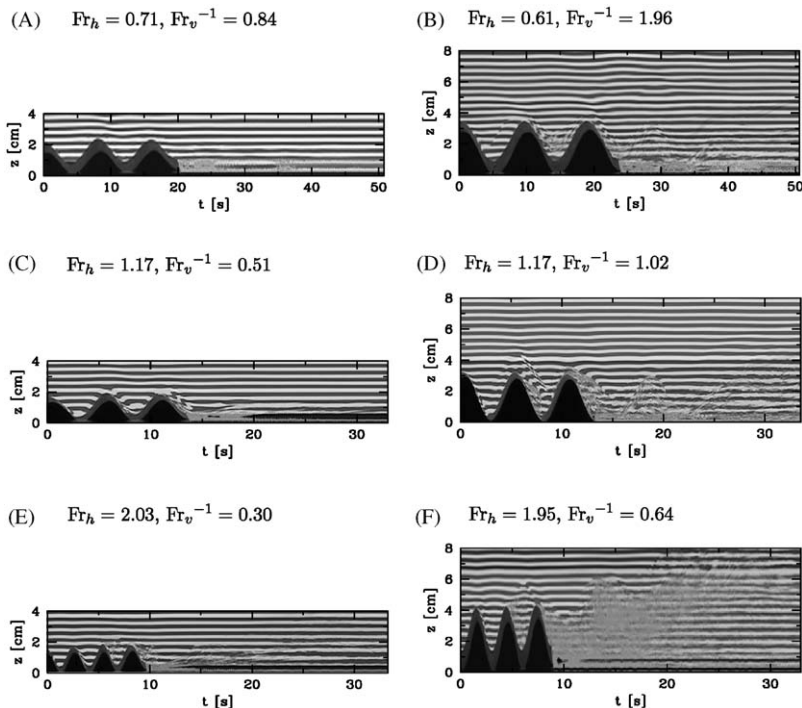

Fig. 7. Sample vertical time series of the near-hill region, illustrating the distortion due to boundary-trapped lee waves and turbulence. The images on the right (B, D, and F) are those for the large-amplitude hills. Boundary-trapped lee waves are generated for a wide range of Fr_h. For large Fr_h, the region in the lee becomes turbulent, although still present is a well-defined boundary-trapped lee wave.

and downstream of a smooth step as observed in a range of experiments by Sutherland (2002).

A similar lee structure is observed at all Fr_h values for the large hills, yet only for select values for the small hills, particularly $Fr_h \gtrsim 1$. For example, a boundary-trapped lee wave is clearly distinguishable in Fig. 7(C) but not in (A).

Figs. 7(D and F) illustrates the effect of increasing Fr_h on the lee structure of the large hills. In particular, as Fr_h increases, the flow in the lee becomes increasingly turbulent. Even so, there remains a coherent boundary-trapped lee wave separating the turbulent mixed regions from the remaining fluid above, the structure of which remains relatively constant.

For the small hills, turbulence is also generated, although to a much smaller extent (compare for example Fig. 7(E) with (F)). As a result, the structure of the boundary-trapped lee wave is more difficult to identify. In all cases where boundary-trapped lee waves are formed, the wave is stationary with respect to the topography. The relationship between the boundary-trapped and resulting vertically propagating internal waves is quantified in Section 4.2.

4. Quantitative results

4.1. Power spectra

Internal wave frequencies and wavenumbers are determined quantitatively from the N_t^2 fields using spectral methods. The choice of whether to use the vertical or horizontal time series depends on the types of wave features present. In particular, for the slower tow-speed experiments, the vertical time series are preferred because they clearly distinguish between the waves generated over and in the lee of the topography, as seen in Fig. 6(B) for example. Thus, windows can be carved from the original time series to isolate the different waves and then spectral methods can be applied separately to each window.

For example, for the time series given in Figs. 6(A and B), a window can be carved from $t = 0$–25 s to isolate the topographically generated waves and from $t = 25$–50 s to isolate the waves generated in the lee. Fig. 8 displays these two windows and the corresponding power spectra obtained by performing a two-dimensional Fourier transform on each of the windows. The location of the peak is used to measure the dominant frequency and vertical wavenumber. In this case, $(\omega, k_z) \approx (0.59, -0.56)$

for the waves over the hills and $(\omega, k_z) \approx (0.61, -0.66)$ for the waves in the lee. By averaging the peak values from time series at eight equally spaced horizontal locations spanning approximately two hill wavelengths, representative values are obtained. For this experiment, these are $\omega = 0.59 \pm 0.06\,\text{s}^{-1}$ and $k_z = -0.59 \pm 0.14\,\text{cm}^{-1}$ for the waves over the hills and $\omega = 0.62 \pm 0.06\,\text{s}^{-1}$ and $k_z = -0.66 \pm 0.14\,\text{cm}^{-1}$ for the waves in the lee, where the uncertainties are set by the resolution of the images.

For faster tow-speed experiments, where large-scale waves are generated in the lee, horizontal time series are preferred. This is because, in many cases, the vertical extent of the waves exceeds the vertical field-of-view and thus, the measurements of k_x are more reliable than those of k_z. Horizontal time series also have the advantage of capturing the movement of waves generated at the same time. Fig. 9 shows a horizontal time series for the experiment of Fig. 6(D), along with its power spectrum. The horizontal time series is taken at a vertical location 15 cm below the peak of the topography. Again, by averaging the peak values of eight equally spaced slices spanning approximately 10 cm, we obtain characteristic values, $k_x = 0.20 \pm 0.10\,\text{cm}^{-1}$ and $\omega = 0.55 \pm 0.09\,\text{s}^{-1}$.

After having determined ω and one of either k_x or k_z, the other wavenumber component can be estimated using the dispersion relation $\omega = Nk_x / \sqrt{k_x^2 + k_z^2}$.

In both Flynn and Sutherland (2004) and Dohan and Sutherland (2003), the estimates of ω and k_x (or k_z) are obtained by further averaging the co-spectrum over all k_x (or k_z) to determine ω and over all ω to determine k_x (or k_z). We found that the values obtained using this method were within the range of uncertainty of those determined from the peaks of the power spectrum. For example, Figs. 9(C and D) gives the averaged k_x and ω profiles determined from the power spectrum in Fig. 9(B). The location of the peaks of these profiles are in agreement with the location of the peak of the power spectrum, as expected. Thus, the results presented in this paper are those obtained from the average peak location of the power spectrum.

4.2. Wave frequencies

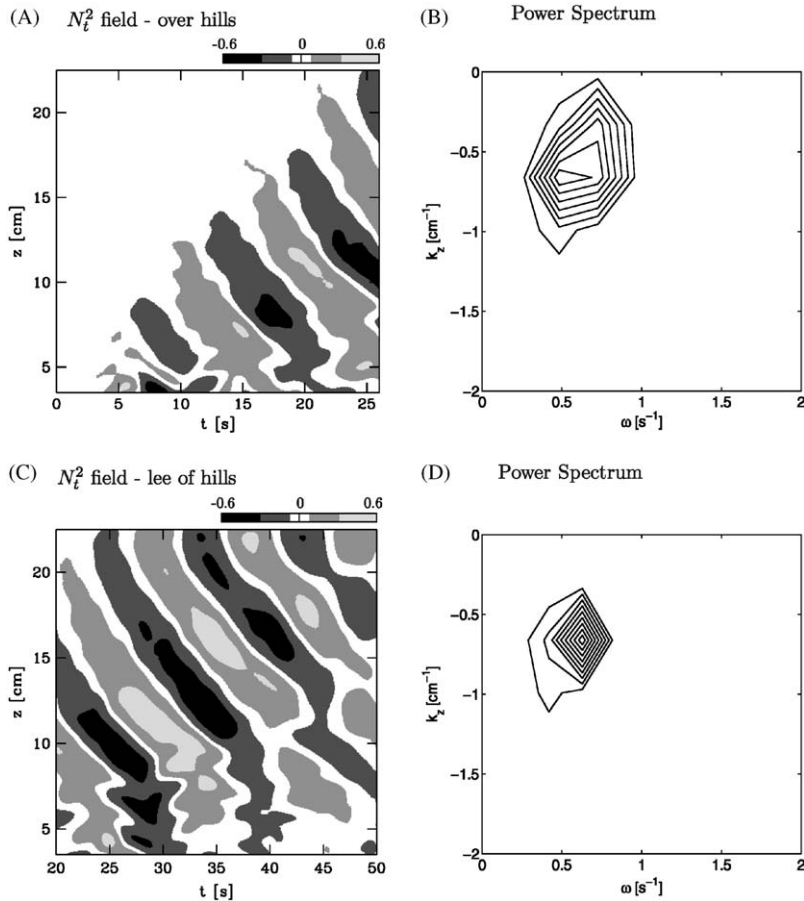Using the methods of the previous subsection, internal wave frequencies are determined for all

Fig. 8. Select windows of the vertical time series of N_t^2 [s^{-3}] for the experiment shown in Fig. 6(B). The window in (A) isolates waves generated directly over the hills, whereas (C) isolates those generated in the lee. In (B) and (D) are the frequency and vertical wavenumber co-spectra determined from the images in (A) and (C), respectively.

experiments. The results are summarized in Fig. 10, which plots the relative internal wave frequency, ω/N, as a function of the relative excitation frequency, $\omega_{\mathrm{exc}}/N = Fr_{\mathrm{h}}$. Solid and open markers distinguish between waves generated directly over the hills and those generated in the lee, respectively. A vertical line clearly distinguishes two regimes, the first of which is termed the "propagation regime" where $Fr_{\mathrm{h}} < 1$. In this regime, we see that the observed frequency of vertically propagating waves over the hills agrees well with the excitation frequency for sufficiently small Fr_{h}, but with significant departures occurring for $0.7 < Fr_{\mathrm{h}} < 1$. Thus, the linear theory prediction is valid for $Fr_{\mathrm{h}} \lesssim 0.7$ even though Fr_{v}^{-1} is of order unity (see Fig. 5) and hence, the forcing mechanism nonlinear. This result holds both for the small- and large-amplitude hills. In this regime we also notice that

the frequency of the waves generated in the lee of the large-amplitude hills matches that of the topographically generated waves, again with significant departure for $0.7 < Fr_{\mathrm{h}} < 1$.

In the "evanescent" regime for which $Fr_{\mathrm{h}} > 1$, propagating waves are no longer generated over the hills but nonetheless occur immediately in the lee of the range. The towing speed is so fast that the fluid does not traverse the valleys but rather flows over them, resembling flow over a single "envelope" of hills or a plateau. This "plateau effect" has been used to describe flow over the coastal terrain of the Western United States and Canada (Braun et al., 1999). To leading order, the waves in the lee are generated as a result of flow down the trailing slope and in this sense resemble the waves generated by flow over a smooth step as examined by Sutherland (2002). As in that study, here we find the wave
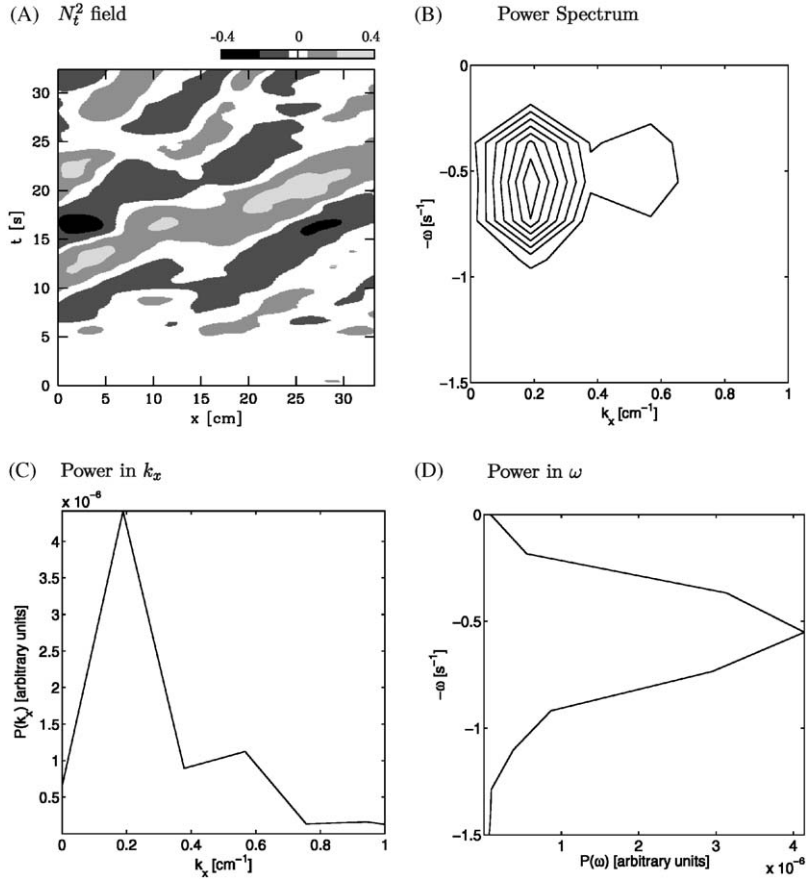
Fig. 9. The frequency and vertical wavenumber spectra and co-spectrum for the experiment shown in Fig. 6(D). In (A) is the horizontal time series of N_t^2 taken at a vertical location 15 cm below the peak of the hills. In (B) is the power co-spectrum determined from (A). The $k_x - \omega$ spectrum is averaged over all ω values, resulting in the k_x-profile given in (C). Similarly, the ω-profile obtained by averaging over all k_x values is given in (D).

frequencies are an approximately constant fraction of the buoyancy frequency, N. In particular, $\omega/N \approx 0.51 \pm 0.02$. One might anticipate the ratio ω/N should be constant: if the horizontal length-scale, L, associated with the generation can be neglected, then the frequency must be determined by N^{-1}, not L/U. It is nonetheless remarkable that the frequency remains constant in the presence of vigorous turbulence and, as we show in Section 5, that the waves persist with this frequency further downstream of the last hill than predicted by Long's model, which neglects turbulence.

As in Sutherland (2002), here we hypothesize that the waves are generated further downstream not only as a consequence of flow over the trailing slope of the envelope topography, but also through coupling with boundary-trapped lee waves. If the propagating and boundary-trapped waves are indeed coupled, we might expect their frequencies to match.

Using vertical time series images, the frequency of a boundary-trapped lee wave, ω_{lee}, is determined approximately by measuring the time between the last hill crest and first crest of the hump-shaped disturbance, as shown, for example, in Fig. 7(D), which gives $T_{lee} \approx 8$ s. Fig. 11 compares the vertically propagating and boundary-trapped lee wave frequencies for all applicable experiments. When $Fr_h < 1$, the frequencies match well. In such cases, $\omega_{lee} \approx \omega \approx \omega_{exc}$. Like the propagating wave frequency, when $Fr_h > 1$ the boundary-trapped lee wave frequency is approximately constant but generally higher than ω/N. This is consistent with the study by Sutherland (2002), which found similar relationships between the propagating and boundary-trapped lee wave frequencies generated by a step-shaped topography.

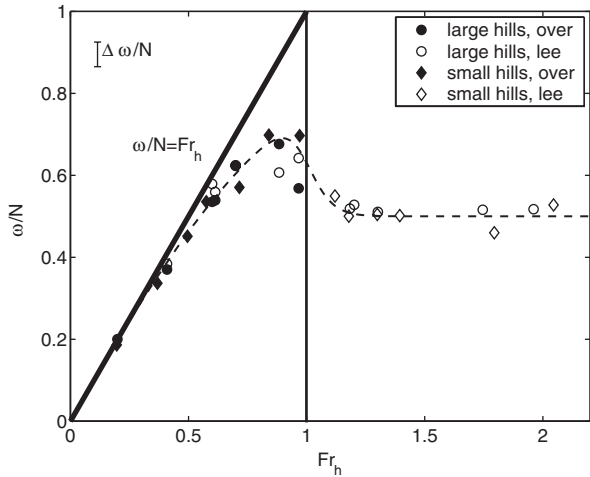As a way of providing a convenient summary of our experimental results, we have fit an empirical

Fig. 10. Plot of measured relative internal wave frequency, ω/N, as a function of relative excitation frequency, $\omega_{exc}/N \equiv Fr_h$. The line $\omega/N = Fr_h$ is plotted to compare the experimental measurements with those predicted by linear theory. The dashed line is an empirical fit to the data.
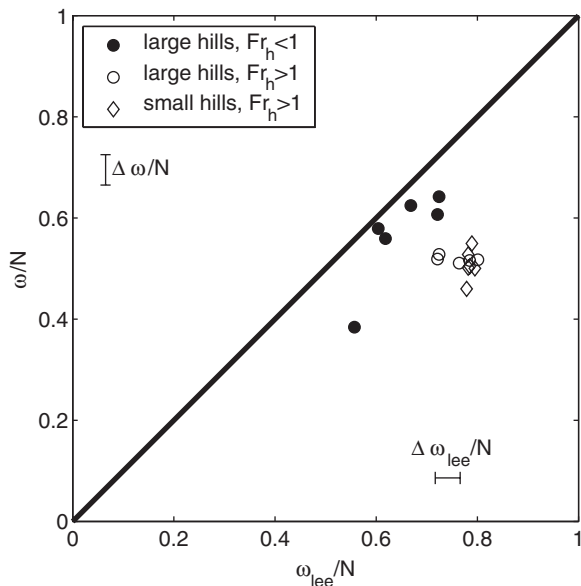

Fig. 11. Comparison of vertically propagating and boundary-trapped lee wave frequencies for experiments in which boundary-trapped lee waves are clearly present.

formula to the frequency data of Fig. 10. The formula is of the form

$$f \approx wf_1 + (1 - w)f_2, \qquad (8)$$

in which f_1 and f_2 describe the behaviour in the subcritical and supercritical regimes, respectively,

and w is a weighting function. Explicitly, the empirical fit to the observed wave frequencies is

$$\omega/N = w[\tanh(Fr_h)] + (1 - w)[0.5], \qquad (9)$$

in which the weighting function is given by

$$w(Fr_h) = 0.5(1 - \tanh[10(Fr_h - 1)]). \qquad (10)$$

The graph of this function is given as a dashed line in Fig. 10. The empirical fit to the data is very good, in most cases well within the uncertainty of the measurements.

4.3. Wave amplitudes

Fig. 12 plots the relative internal wave amplitudes, $2A_\xi/H$, as a function of the horizontal Froude number, Fr_h. As in Fig. 10, a vertical line divides the plot into two regimes and a thick horizontal line gives the linear theory prediction. Although linear theory predicts that the amplitudes of the waves generated over the hills should equal the hill amplitude for $Fr_h < 1$, this is clearly not the case. The wave amplitudes are significantly smaller, even for those generated over the small hills and especially for those generated over the large hills. This is an indication that nonlinear processes are important even for relatively smooth topography with $H/\lambda = 0.1$.

We saw earlier (Fig. 7(B)) for a case of $Fr_h < 1$ and $H/\lambda = 0.2$ that fluid separated from the lee-side slopes of each hill and formed patches of trapped fluid in the valleys. This reduced the effective hill
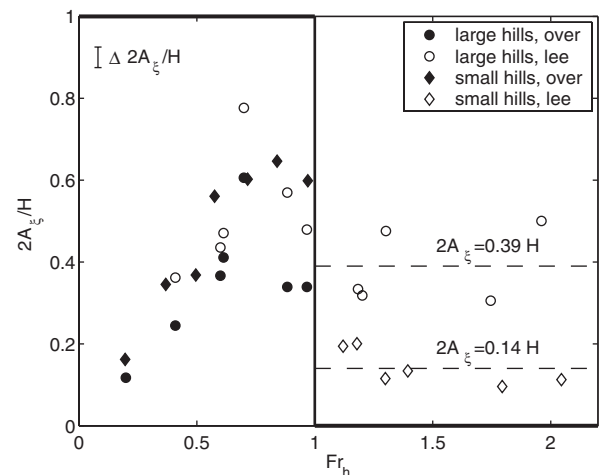

Fig. 12. Plot of normalized internal wave amplitude, $2A_\xi/H$, as a function of Fr_h. The thick horizontal lines give the amplitude predicted by linear topographic forcing. The dashed lines give the average amplitude values for each hill height for $Fr_h > 1$.

height. The important parameter that determines such separation is $Fr_v^{-1} = NH/U$. This parameter increases with increasing H or decreasing U, both of which contribute to generating adverse pressure gradients allowing for boundary-layer separation.

In our experiments (with the exception of one anomaly), the experiments with $Fr_v^{-1} > 1$ and thus, $Fr_h < 1$ according to Fig. 5, generated waves over the hills having the smallest amplitudes, $2A_\xi \lesssim 0.4H$. It is in these cases that the nonlinear process of boundary-layer separation dominates and significantly reduces the effective hill height. The majority of these experiments are for the large hills where we would expect nonlinear effects to be greater.

Fig. 13 presents vertical time series of the near-hill region for the experiments with the highest Fr_v^{-1} values ($Fr_v^{-1} \gtrsim 3$). In these cases, the effects of boundary-layer separation and flow blocking are most extreme and the resulting wave amplitudes are lowest. Comparing Fig. 13(A) with (B), increasing H acts to increase the height of the blocked layer, while maintaining a relatively constant effective hill height as far as wave generation is concerned. This is consistent with the constancy of H_{eff} found by

Welch et al. (2001). In experiments with larger towing speeds and thus smaller Fr_v^{-1} (Fig. 13(C)), separation still occurs but further downstream the lee slope compared with that in Fig. 13(B). The experiments show that for fixed Fr_h, Fr_v^{-1} limits the effective hill height and thus, the amplitudes of waves generated over the hills.

Apart from the waves generated over the hills, Fig. 12 also gives the amplitudes of the waves generated in the lee of the hills, which result from flow over the lee-side slope of the last hill and the boundary-trapped lee wave as discussed earlier. For $Fr_h < 1$, only those waves generated in the lee of the large hills are included. This is because the small hills failed to generate well-defined boundary-trapped lee waves and as a result, the amplitude of the wave field increased only slightly in the lee. From Fig. 12, the amplitudes of the waves generated in the lee of the large hills are greater than those generated over the hills, varying from 10–40% greater. This is expected because the waves are generated in part by flow over the larger-amplitude boundary-trapped lee waves.

In the supercritical regime ($Fr_h > 1$), the propagating lee wave amplitudes remain large for the large-amplitude hills ($2A_\xi/H \approx 0.39 \pm 0.20$) but decrease significantly for the small-amplitude hills ($2A_\xi/H \approx 0.14 \pm 0.09$). These average values are presented as dashed lines in Fig. 12. Because the propagating and boundary-trapped lee wave frequencies do not match in this case (Fig. 11), we conclude that the waves are generated by a combination of flow over envelope topography and the boundary-trapped lee wave. We know the boundary-trapped lee wave continues to play a significant role because the propagating wave amplitudes are larger for the large-amplitude hills and the corresponding boundary-trapped lee waves also have significantly larger amplitudes (compare, for example, Fig. 7(E) with (F)).

4.4. Analysis

The vertical flux of horizontal momentum, $\mathscr{F}_{\text{uw}}$, can be determined using the measured amplitudes and frequencies according to linear theory

$$\mathscr{F}_{\text{uw}} = \tfrac{1}{4}\rho_0 N^2 \sin(2\Theta) A_\xi^2. \tag{11}$$

The momentum fluxes for a range of experiments are plotted as a function of the horizontal Froude number in Fig. 14. Here, the measured fluxes, $\mathscr{F}_{\text{meas}}$, are normalized by the maximum flux
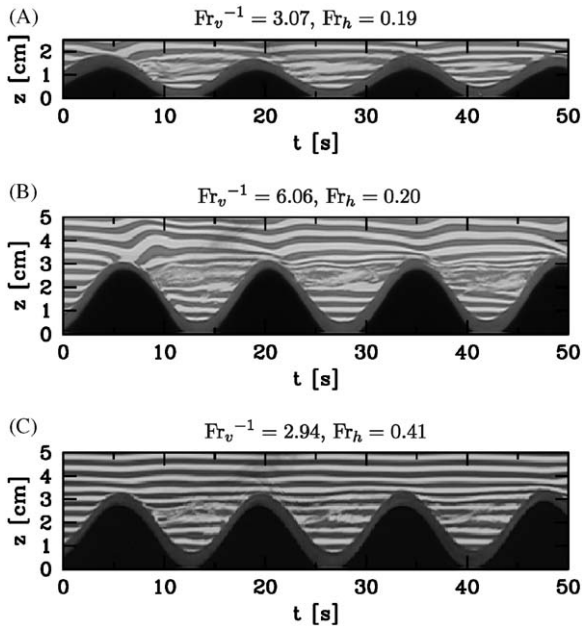

Fig. 13. Vertical time series images of the near-hill region for experiments with large Fr_v^{-1}. The effects of flow separation and consequent trapping of fluid in the valleys are evident in all cases. The height of the blocked layer increases with increasing H (compare (A) with (B)) and decreases with increasing U (compare (B) with (C)).
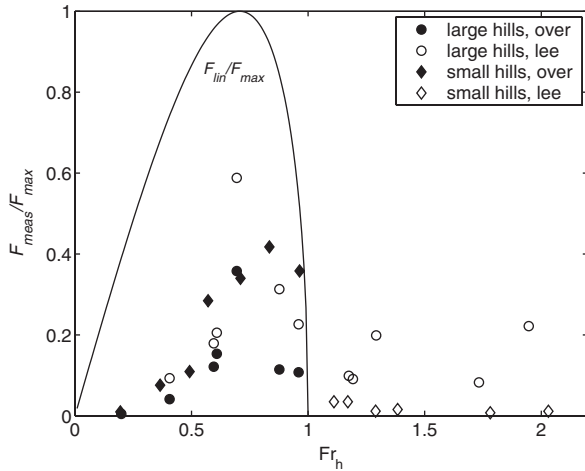
Fig. 14. Plot of normalized vertical flux of horizontal momentum, $\mathscr{F}_{\text{meas}}/\mathscr{F}_{\text{max}}$, as a function of Fr_h. The measured flux, $\mathscr{F}_{\text{meas}}$, is normalized by a characteristic value of linear internal wave theory, $\mathscr{F}_{\text{max}} = \frac{1}{4}\rho_0 N^2 (H/2)^2$. A curve representing the flux predicted by linear theory is plotted for reference.

Fig. 15. Plot of relative wave amplitude, A_ξ/λ_x, as a function of the angle of wave propagation to the vertical, Θ. The curve denoted "SA" is the critical relative amplitude at which the waves should become unstable by self-acceleration. The curve denoted "OT" is the relative amplitude at which the waves should overturn.

predicted by linear theory, $\mathscr{F}_{\text{max}} = \frac{1}{4}\rho_0 N^2 (H/2)^2$. A curve representing the momentum flux that would result if $A_\xi = H/2$ is provided for reference. The general trends are similar to those of Fig. 12. Note that the measured values are consistently below the theoretical values for $Fr_h < 1$. Due to their larger amplitudes for $Fr_h > 1$, the waves generated from the large-amplitude hills are able to transport momentum where linear theory predicts there to be no waves.

As a way of summarizing the amplitude and frequency results presented thus far, we present them in the form of a stability diagram in Fig. 15 (Flynn and Sutherland, 2004; Dohan and Sutherland, 2003). This figure includes the critical amplitudes for two types of internal-wave instabilities, namely overturning (denoted "OT") and self-acceleration (denoted "SA"). Overturning refers to the instability that occurs when dense fluid overlies less dense fluid. The critical relative amplitude for this instability is given by

$$A_{\text{OT}} = \frac{1}{2\pi} \cot \Theta. \tag{12}$$

Self-acceleration occurs when the wave-induced mean flow approaches the horizontal group velocity of the waves. The effect is to alter wave propagation and particularly, increase wave amplitude. When the wave-induced mean flow exceeds the horizontal group velocity, then the waves may become unstable
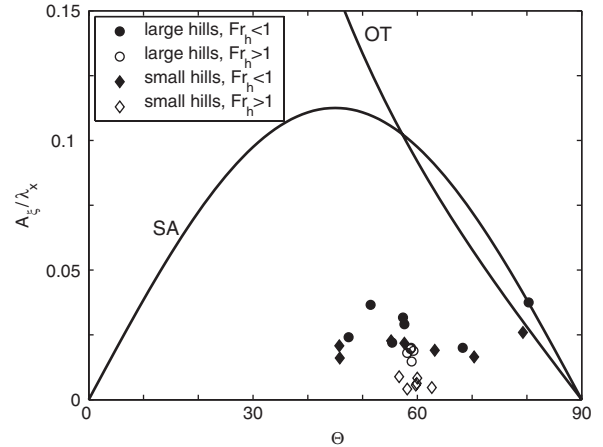
and break. The critical relative amplitude for this instability is given by (Sutherland, 2001)

$$A_{\text{SA}} = \frac{1}{2\pi\sqrt{2}} \sin 2\Theta. \tag{13}$$

There are two main observations to be made from Fig. 15. First of all, with the exception of the open triangles, the waves are relatively large in the sense that the wave amplitudes are 2–4% of the horizontal wavelengths and 20–40% of the breaking amplitudes. Secondly, for the case of $Fr_h > 1$, the angles of propagation to the vertical lie in a very narrow range about $\Theta \approx 58°$, corresponding to the narrow frequency range. Such a narrow range has been observed in other studies involving the dynamic generation of internal waves, as summarized in Table 1. In particular, the results from flow over boundary-trapped lee waves are similar to those of Sutherland and Linden (1998) and Flynn and Sutherland (2004), who studied stratified flow past a thin barrier and intrusive gravity currents, respectively. The resulting mechanism of wave generation in both cases was similar to that observed in our experiments, in particular flow over an undular coherent structure.

5. Comparison with Long's model

Here we compare the theoretical results of Long's model (Long, 1953) with our experiments. Long's

Table 1
Comparison of angle of wave propagation and relative wave amplitude for five studies involving the dynamic generation of internal gravity waves

Study	Mechanism of wave excitation	$\Theta(^\circ)$	A_ζ/λ_x
Linden (1975)	Stationary turbulence	≈ 35	N/A
Sutherland and Linden (1998)	Turbulent shear flow	46–60	0.003–0.03
Dohan and Sutherland (2003)	Stationary turbulence	42–55	0.02–0.04
Flynn and Sutherland (2004)	Intrusive gravity current	41–64	0.005–0.02
Present study	Boundary-trapped lee waves	57–63	0.01–0.03

model is an equation for the steady streamfunction perturbed due to flow over topography of arbitrary amplitude. As such, it is an improvement over linear theory which, strictly speaking, is applicable only for wave generation from infinitesimally small amplitude hills. Even so, we do not expect excellent agreement between Long's model and our experiments because the model assumes the flow over topography is steady, inviscid, and free-slip, and so does not take into account the initial transient development of the waves, boundary layer separation, trapping of dense fluid in valleys, and the generation of turbulence.

Despite these limiting assumptions, the model has been used, for example, as an initial condition for numerical simulations examining upper-level internal wave breaking in the atmosphere above isolated topography and the consequent generation of downslope winds (Laprise and Peltier, 1989; Scinocca and Peltier, 1989). Although these simulations assumed inviscid flow, and hence neglected boundary layer separation, this assumption is not necessarily valid for topography having steep slopes or topography consisting of two or more hills whereby dense fluid can be trapped in the valleys. Even in the case where the flow is relatively fast, and Fr_v^{-1} small, we have seen that boundary layer separation results in the shedding of coherent turbulent structures in the lee of steep hills, which alters wave generation.

The purpose of this section is to compare the predictions of Long's model against our laboratory experiments and thereby to further examine the role of boundary layer separation in these moderately large Reynolds number flows.

Explicitly, Long's model for steady, two-dimensional flow of uniformly stratified fluid, characterized by constant buoyancy frequency N_0, moving with uniform upstream speed, U_0, over topography

is given by the Helmholtz equation

$$\psi_{xx} + \psi_{zz} + \left(\frac{N_0}{U_0}\right)^2 \psi = 0, \tag{14}$$

in which ψ is the perturbation streamfunction and the subscripts denote partial derivatives. Although (14) is a linear partial differential equation, it nonetheless describes finite-amplitude effects, which enter through the specification of nonlinear boundary conditions. In particular, assuming an inviscid, free-slip lower boundary, we require that the surface is itself a streamline, which arbitrarily we set to zero. Thus we require

$$-U_0 h(x) + \psi(x, h(x)) = 0, \tag{15}$$

in which we have evaluated the background streamfunction, $\Psi(z) \equiv -U_0 z$, and the perturbation streamfunction, $\psi(x, z)$, at the height of the topography, $z = h(x)$.

For the generation of small-amplitude, hydrostatic internal waves, Eqs. (14) and (15) may be solved by standard Fourier methods:

$$\psi(x, z) = \int_{-\infty}^{\infty} \eta(k) e^{i[kx + m(k)z]} \, dk, \tag{16}$$

in which $m^2 = -k^2 + N_0^2/U_0^2$ (with the appropriate branch cut taken when computing m so that waves are outward propagating), and $\eta(k)$ is found from the linearized boundary condition

$$U_0 h(x) \simeq \psi(x, 0) = \int_{-\infty}^{\infty} \eta(k) e^{ikx} \, dk. \tag{17}$$

For large amplitude disturbances, assuming the streamfunction ψ retains the form in (16), the exact boundary condition is

$$U_0 h(x) = \int_{-\infty}^{\infty} \eta(k) e^{i[kx + m(k)h(x)]} \, dk. \tag{18}$$

This is a Fredholm integral equation of the first kind that determines the Fourier coefficients $\eta(k)$ from the topographic profile $h(x)$. Generically, first-kind integral equations are ill-conditioned and, consequently, numerical discretization leads to large linear systems whose matrices are poorly conditioned. Nonetheless, if the flow is nearly hydrostatic ($Fr_h \ll 1$), reasonable numerical solutions can be obtained (see, for example, Llewellyn Smith and Young, 2003; Petrelis et al., 2005). In nonhydrostatic cases, the ill-conditioning cannot be overcome and a different numerical approach is necessary. Recently, Muraki (2005) has recast Long's model into an integral equation of the second-kind. Numerical discretization of second-kind problems yield matrices which are typically diagonally dominant and thus are better conditioned.

The solutions of Long's model under the conditions of the two small-amplitude hill experiments shown in Figs. 6(A and B) are presented in Fig. 16. Fig. 16(A) is computed using the solution method for integral equations of the first-kind, which gives good convergence for this small value of Fr_h. The method for second-kind integral equations is used to compute the solutions shown in Fig. 16(B), in which the waves are significantly nonhydrostatic. Both are the steady-state solutions for flow over 4 sinusoidal hills and, for ease of comparison, the results are presented as vertical time series rather than spatial snapshots.

Qualitatively, Long's model captures the features we observe in these two experiments. In the case with $Fr_h < 1$ (Fig. 16(A)), vertically propagating waves are generated with upstream phase tilt and

waves in the lee have slightly larger amplitude than those over topography. In the case with $Fr_h > 1$ (Fig. 16(B)), waves immediately above the topography are evanescent but a transient burst of vertically propagating waves appears in the lee of the last hill.

Although good qualitative agreement is found, Long's model predicts that the wave amplitude is significantly larger than observed in experiments. Note, for example, that the range of the colour contours is 10 times larger in Fig. 16(A) than in the corresponding plot in Fig. 6(A). Furthermore, the streamlines in Fig. 16(A) are overturning, although overturning is not observed in the experiment. Likewise, though not shown here, Long's solution computed for the large-amplitude experiments shown in Figs. 6(B and D) predicts the generation of waves of much larger amplitude than are actually observed. Also, waves are predicted to be overturning, though this is not what we find in experiments with the large-amplitude hills.

A simple linear theory calculation predicts that overturning above infinitely periodic sinusoidal hills with half peak-to-peak hill height, $H/2$, should occur if

$$\frac{H}{2} > \frac{\lambda}{2\pi} \frac{Fr_h}{\sqrt{1 - Fr_h^2}}. \tag{19}$$

For the experiment shown in Fig. 6(A), this overturning condition becomes $H/2 \gtrsim 0.11\lambda$. The small-amplitude hills in fact satisfy $H/2 = 0.047\lambda$, well below the overturning amplitude. There are two reasons why Long's model nonetheless predicts overturning. First, the hills have finite horizontal
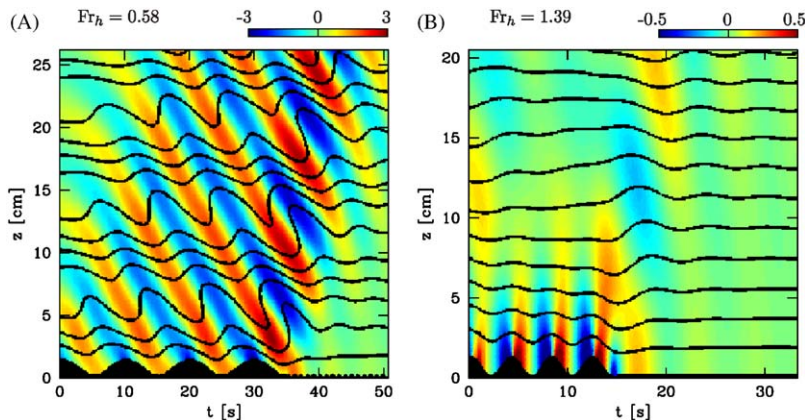

Fig. 16. Long's model solution for (A) subcritical and (B) supercritical forcing corresponding to the experiments shown in Figs. 6(A) and (C), respectively. The colour contours show values of N_t^2 [s^{-3}], though the ranges differ from those in Fig. 6. The black lines are streamlines.

extent and the flow at the bottom boundary approaching from infinity is at the same vertical level as the bottom of the valleys, not the mid-depth between hill crests and valleys. Thus the flow is displaced by the peak-to-peak distance, not half that value. Second, nonlinear dispersive effects, such as self acceleration, act to increase the amplitude of the waves further so that they become overturning.

We might then expect to see overturning in the laboratory experiments and yet, we do not. The primary reason is that Long's model does not permit boundary-layer separation: the wave amplitude in the model is set directly by the hill height. Thus, the amplitude of waves generated in experiments is smaller because the flow over topography does not penetrate down to the bottom of the valleys between the hills but rather, fluid remains stagnant close to the valley floors. Likewise, Long's model does not predict the generation of boundary-trapped lee waves and turbulence. Therefore, it does not account for the modification of propagating waves in the lee by these phenomena. Another reason we do not see overturning in the laboratory experiments may be due to columnar motions, which have been observed to oppose the steepening of the lee waves and to increase the value of Fr_v^{-1} above which overturning occurs from that predicted by Long's model (Baines and Hoinka, 1985).

6. Discussion and conclusions

We have investigated internal wave generation over sinusoidal topography and compared our results with linear theory and the finite-amplitude predictions of Long's model. For slow towing speeds ($Fr_\mathrm{h} < 1$), measured wave frequencies agree well with the excitation frequencies predicted by linear theory provided $Fr_\mathrm{h} \lesssim 0.7$. However, linear theory significantly overestimates wave amplitudes, even for the small-amplitude hills with $H/\lambda \approx 0.1$. This is also true for Long's model and can be explained by boundary-layer separation, which acts to reduce the effective hill height. The generation of large-amplitude waves in the lee of the large-amplitude hills is also observed and couples with boundary-trapped lee waves. In particular, $\omega \approx \omega_\mathrm{lee}$ in a range from 0.55 to 0.75N. This is the same range observed by Sutherland (2002) for experiments using a large-amplitude step with $Fr_\mathrm{v}^{-1} > 1$.

At supercritical towing speeds, propagating internal waves are observed in the lee of the topography. These waves, generated in part through excitation by envelope topography, also weakly couple with coherent turbulent structures in the lee, called boundary-trapped lee waves. Both the propagating and boundary-trapped lee waves are excited within a narrow range of frequencies, with $\omega < \omega_\mathrm{lee}$ in general.

Future work will examine flow over large-amplitude rough topography, in particular over a series of rectangular and triangular hills. It is expected that turbulence between and in the lee of the hills will be the dominant mechanism of wave generation. The results will be compared and contrasted with those of the present study, ultimately working towards increasing our understanding of internal wave generation over finite-amplitude periodic topography, including the effects of turbulence.

References

Baines, P.G., 1995. Topographic Effects in Stratified Flows. Cambridge University Press, Cambridge.

Baines, P.G., Hoinka, K.P., 1985. Stratified flow over two-dimensional topography in fluid of infinite depth: a laboratory simulation. Journal of the Atmospheric Sciences 42, 1614–1630.

Balmforth, N.J., Ierley, G.R., Young, W.R., 2002. Tidal conversion by subcritical topography. Journal of Physical Oceanography 32, 2900–2914.

Braun, S.A., Rotunno, R., Klemp, J.B., 1999. Effects of coastal orography on landfalling cold fronts. Part I: dry, inviscid dynamics. Journal of the Atmospheric Sciences 56, 517–533.

Carruthers, D.J., Hunt, J.C.R., 1986. Velocity fluctuations near an interface between a turbulent region and a stably stratified layer. Journal of Fluid Mechanics 165, 475–501.

Dalziel, S.B., Hughes, G.O., Sutherland, B.R., 2000. Whole field density measurements. Experiments in Fluids 28, 322–335.

Dohan, K., 2004. Internal wave generation from a turbulent mixed region. Ph.D. Thesis, University of Alberta, Canada.

Dohan, K., Sutherland, B.R., 2003. Internal waves generated from a turbulent mixed region. Physics of Fluids 15, 488–498.

Flynn, M.R., Sutherland, B.R., 2004. Intrusive gravity currents and internal gravity wave generation in stratified fluid. Journal of Fluid Mechanics 514, 355–383.

Garabato, A.C.N., Polzin, K.L., King, B.A., Heywood, K.J., Visbeck, M., 2004. Widespread intense turbulent mixing in the Southern Ocean. Science 303 (5655), 210–213.

Klymak, J.M., Gregg, M.C., 2004. Tidally generated turbulence over the Knight Inlet sill. Journal of Physical Oceanography 34 (5), 1135–1151.

Lamb, K.G., 2004. Nonlinear interaction among internal wave beams generated by tidal flow over supercritical topography. Geophysical Research Letters 31, doi:10.1029/2003GL019393.

Laprise, R., Peltier, W.R., 1989. On the structural characteristics of steady finite-amplitude mountain waves over bell-shaped topography. Journal of the Atmospheric Sciences 46 (4), 486–495.

Ledwell, J.R., Montgomery, E.T., Polzin, K.L., Laurent, L.C.S., Schmitt, R.W., Toole, J.M., 2000. Evidence of enhanced mixing over rough topography in the abyssal ocean. Nature 403, 179–182.

Linden, P.F., 1975. The deepening of a mixed layer in a stratified fluid. Journal of Fluid Mechanics 71, 385–405.

Llewellyn Smith, S.G., Young, W.R., 2002. Conversion of the barotropic tide. Journal of Physical Oceanography 32, 1554–1566.

Llewellyn Smith, S.G., Young, W.R., 2003. Tidal conversion at a very steep ridge. Journal of Fluid Mechanics 495, 175–191.

Long, R.R., 1953. Some aspects of the flow of stratified fluids. A theoretical investigation. Tellus 5, 42–58.

Muraki, D.J., 2005. The large amplitude wave solutions of Long's theory for 2D topographic flow. Journal of the Atmospheric Sciences, in preparation.

New, A.L., DaSilva, J.C.B., 2002. Remote-sensing evidence for the local generation of internal soliton packets in the central Bay of Biscay. Deep-Sea Research I 49 (5), 915–934.

Oster, G., 1965. Density gradients. Scientific American 213, 70.

Petrelis, F., Llewellyn Smith, S.G., Young, W.R., 2005. Tidal conversion at a submarine ridge. Journal of Physical Oceanography, in press.

Rudnick, D.L., Boyd, T.J., Brainard, R.E., Carter, G.S., Egbert, G.D., Gregg, M.C., Holloway, P.E., Klymak, J.M., Kunze, E., Lee, C.M., Levine, M.D., Luther, D.S., Martin, J.P., Merrifield, M.A., Moum, J.N., Nash, J.D., Pinkel, R., Rainville, L., Sanford, T.B., 2003. From tides to mixing along the Hawaiian ridge. Science 301 (5631), 355–357.

Scinocca, J.F., Peltier, W.R., 1989. Pulsating downslope windstorms. Journal of the Atmospheric Sciences 46, 2885–2914.

St. Laurent, L., Garrett, C., 2002. The role of internal tides in mixing the deep ocean. Journal of Physical Oceanography 32, 2882–2899.

St. Laurent, L., Stringer, S., Garrett, C., Perrault-Joncas, D., 2003. The generation of internal tides at abrupt topography. Deep-Sea Research I 50 (8), 987–1003.

Sutherland, B.R., 2001. Finite-amplitude internal wavepacket dispersion and breaking. Journal of Fluid Mechanics 429, 343–380.

Sutherland, B.R., 2002. Large-amplitude internal wave generation in the lee of step-shaped topography. Geophysical Research Letters 29(16), doi:10.1029/2002GL015321.

Sutherland, B.R., Linden, P.F., 1998. Internal wave excitation from stratified flow over a thin barrier. Journal of Fluid Mechanics 377, 223–252.

Sutherland, B.R., Dalziel, S.B., Hughes, G.O., Linden, P.F., 1999. Visualization and measurement of internal waves by synthetic schlieren. Part 1: vertically oscillating cylinder. Journal of Fluid Mechanics 390, 93–126.

Welch, W., Smolarkiewicz, P., Rotunno, R., Boville, B.A., 2001. The deepening of a mixed layer in a stratified fluid. Journal of the Atmospheric Sciences 58 (12), 1477–1492.